Thermionic emission from monolayer graphene, sheath formation and its feasibility towards thermionic converters

Shikha Misra,[1,2,a)] M. Upadhyay Kahaly,[3] and S. K. Mishra[3]

[1]*Centre for Energy Studies (CES), Indian Institute of Technology Delhi (IITD), New Delhi, India*
[2]*F-32, CSIR-CEERI, Col., Pilani, India*
[3]*ELI-ALPS, Szeged, Hungary*

A formalism describing the thermionic emission from a single layer graphene sheet operating at a finite temperature and the consequent formation of the thermionic sheath in its proximity has been established. The formulation takes account of two dimensional densities of state configuration, Fermi-Dirac (*f-d*) statistics of the electron energy distribution, Fowler's treatment of electron emission, and Poisson's equation. The thermionic current estimates based on the present analysis is found to be in reasonably good agreement with experimental observations (Zhu *et al.*, Nano Res. **07**, 1 (2014)). The analysis has further been simplified for the case where *f-d* statistics of an electron energy distribution converges to Maxwellian distribution. By using this formulation, the steady state sheath features, viz., spatial dependence of the surface potential and electron density structure in the thermionic sheath are derived and illustrated graphically for graphene parameters; the electron density in the sheath is seen to diminish within ~10 s of Debye lengths. By utilizing the graphene based cathode in configuring a thermionic converter (TC), an appropriate operating regime in achieving the efficient energy conversion has been identified. A TC configured with the graphene based cathode (operating at ~1200 K/work function 4.74 V) along with the metallic anode (operating at ~400 K/ work function 2.0 V) is predicted to display ~56% of the input thermal flux into the electrical energy, which infers approximately ~84% of the Carnot efficiency. *Published by AIP Publishing.* [http://dx.doi.org/10.1063/1.4975788]

I. INTRODUCTION AND MOTIVATION

The direct and efficient conversion of thermal energy (heating) into electricity offers a potential alternative energy resource in addition to available conventional sources and is of technological relevance to power plants, industries, and numerous space applications.[1–10] In the conventional conversion process, the thermionic (TI) electrons from the cathode (emitter) carrying sufficient thermal energy are collected over the anode plate (collector) through a resistive load to utilize it as an electrical power.[4] The applicability of such energy conversion devices is constrained by low conversion efficiency[4] due to (i) lack of TI materials operating at high temperature and (ii) in overcoming the effect of space charge limited scenarios.[10–15] Thus, compact designing and optimization of TI materials that can withstand at a large temperature difference are essential.[16–18] Numerous materials have been proposed,[19–22] which can efficiently operate at high temperature without changing their inherent statistical features; in fact, in a recent work, boron-rich cluster[23] has experimentally been verified to tolerate temperature as high as ~2000 K. The feasibility of the material sheet to operate at higher temperature significantly increases the thermionic electron flux from the cathode, depleting at a collector plate, which in turn might certainly enhance the efficacy of thermionic converters (TCs).

Among many advanced materials, tightly packed thin layered honeycomb carbon atom lattice termed graphene has attained huge attention from the scientific community[24] due to its unique features like light weight with high stiffness, ultrahigh electrical conductivity, extreme mobility, and linear band structure;[24–26] graphene, in fact, is referred as the basis of graphite, graphene ribbon, quantum dots, carbon nano-tubes (CNTs), etc. At present, large scale graphene sheets are commercially available for ample application in the horizon of electronics, biotechnology, and many other streams.[27–32] The intriguing features of graphene are primarily stimulated by the availability of free electron in its truly linear band structure near Fermi level and widely deviate from its usual counterpart bulk material and other allotropic structures.[33–37] A thin layered graphene provides additional flexibility of tuning the intrinsic Fermi level relative to the Dirac point at the desired level by adjusting its chemical potential across the sheet[38] and intrinsic Fermi energy is seen to display the linear temperature dependence.[39] In recent studies,[40–46] the electronic properties driven by electron emission from crystalline carbon allotropes (CNTs) is shown to be significantly different from bulk graphite. In an elegant work,[47] the thermionic emission from a few-layer graphene has been investigated and the transition of its behavior from usual bulk T^2 (Richardson Dushman law) to T^3 dependence, has been specified by a simple relation. In order to physically interpret these effects, the present understanding of the electron emission needs to be revised by taking the unique features and energy states of graphene (mono/multi layered atomic sheets) into account.

a)E-mail: shikhamish@gmail.com

Concerning the applicability of graphene at high temperature ($\sim$1500 K), we analyze the thermionic emission from the single (monoatomic) layered graphene sheet operating at finite temperature, along with steady state sheath formation via thermionic electrons. Graphene also offers an ease to access the planar region of high electron density with ultra-high mobility which can be aligned into direct current towards the collector plate in optimizing the conversion efficiency in TCs. Thus, it is also of interest to examine the feasibility of a monoatomic graphene sheet, whether it could be a viable contraption in search of efficient TCs. In this framework, the two specific aspects associated with the thermionic emission from the monoatomic 2-d graphene sheet operating at finite temperature, which have been considered here in the analysis, are as follows:

(i) Thermionic sheath formation in vacuum: In steady state, the continuous flow of thermionic electrons and their recombination on the graphene surface in vacuum lead to its surface to acquire finite positive potential and consequent formation of a thermionic electron sheath in the proximity of the graphene surface. The thermionic emission from the graphene sheet has been taken up in a recent work but its analysis is constrained to the Maxwellian distribution of electrons and applicable to a high temperature regime[48] only. In the present analysis, following Fowler's approach[49] along with an appropriate configuration of density of states inside the infinitesimally thin two dimensional (2-d) graphene sheet and taking the Fermi Dirac (f-d) statistics for the energy distribution of electrons inside, the expressions for the thermionic emission have been derived; along with this, the linear temperature dependence of the intrinsic Fermi level[39] has also been considered. The consistency of the analytical expressions for current density has further been verified with recent experimental measurements.[50] Furthermore, by utilizing Poisson's equation in the sheath (thermionic cloud) region, a formalism to evaluate the steady state structure of the thermionic sheath on the monoatomic (single layered) graphene sheet has been formulated and its dependence on numerous graphene parameters has been discussed. *(ii) Utility of graphene sheet towards TCs as cathode*: After the knowledge of the thermionic emission flux from the monoatomic (single layered) graphene sheet, it is interesting to exploit its applicability towards the thermionic converters (TCs). The viability of graphene sheets to operate at higher temperature and advanced surface engineering has put forward an option for it to be utilized as a graphene based cathode[30–32] in the thermionic conversion process. In a TC configuration,[4] the cathode (emitter) plate is usually kept at a higher temperature and negative bias with respect to the collector (anode) plate maintained at a lower temperature; the electrical circuit is completed via an external load giving electrical power as the output. In this process, the electron flux is transported from higher Fermi level of the cathode to lower Fermi level of the anode and the remainder is converted into the electrical power (radiation and other losses being small). Mimicking the TC configuration as a combination of the graphene based cathode (emitter) and metal based collector (anode), the conversion efficiency of TC as a function of graphene parameters has been investigated. The effect of space charge in TC configuration has been incorporated as an additional potential barrier in the emitter flux and its effect on the conversion efficiency has also been evaluated.

The organization of the paper is as follows: Section II is devoted to the analysis of thermionic emission and consequent sheath formation (in the steady state) over an infinitesimally thin (monoatomic) graphene sheet. The feasibility of this formulation towards thermionic conversion has been established in Section III. The physics interpretation of the numerical results based on the analytical formulation/expressions has been discussed in Section IV, while a summary of the outcome of this analysis in Section V concludes the paper.

II. ANALYSIS

A. Thermionic emission from infinitesimal thin sheet (monoatomic layer graphene structure)

According to Wallace's[51] theory for graphene like fine structures, the electrons in the fine sheet exhibits a Fermionic character and follows Fermi-Dirac statistics inside the sheet. In this 2-d sheet (say *yz* plane) framework, the electrons exhibit in a low energy quantum regime with quantized parallel energy $E_t = \hbar v_f k$, where v_f refers to the velocity of massless Dirac fermions in graphene.[48] The number of electronic states per unit cell of energy lying between E_t and $(E_t + dE_t)$ can thus be written as[52,53]

$$\rho(E_t)dE_t = [2/(2\pi)^2]dk_y dk_z = [2/(2\pi)^2]2\pi k_t dk_t$$
$$= [1/\pi(\hbar v_f)^2]E_t dE_t. \tag{1a}$$

The number of electrons hitting the top layer (available for emission) from inside, having total energy between E and $(E + dE)$ and normal energy between E_x and $(E_x + dE_x)$ can thus be written as[48]

$$n_{e,fd}(E, E_x)dEdE_x = [1/\pi(\hbar v_f)^2]E_t(2mE_x)^{1/2}f_{FD}(E)dE_x dE$$
$$\Rightarrow n_{e,fd}(\varepsilon, \varepsilon_x)d\varepsilon d\varepsilon_x = (\beta_0/e)T^3(m/2kT)^{1/2}\varepsilon_x^{-1/2}$$
$$\times (\varepsilon - \varepsilon_x)f_{FD}(\varepsilon)d\varepsilon d\varepsilon_x, \tag{1b}$$

where $\beta_0 = (ek^3/\pi\hbar^3 v_f^2)$, $f_{FD}(\varepsilon) = [1 + \exp(\varepsilon - \varepsilon_F)]^{-1}$ refers to the Fermi Dirac distribution,[54] m is the electronic mass, $\hbar$ and k correspond to Planck's and Boltzmann's constants, $\varepsilon_x = E_x/kT = \hbar^2 k^2/2mkT$, $\varepsilon_t = E_t/kT$, $\varepsilon_t = E_t/kT$, $\varepsilon_F = E_F/kT$, E_F refers to the intrinsic Fermi energy level relative to the Dirac point, and T is the temperature of the emitting surfaces; in the case of graphene sheet[55] $v_f = 1.1 \times 10^6$ m/s and $\beta_0 \sim 92$ A/m^2 K^3.

The net electron density estimate can be obtained by integrating over appropriate limits and algebraic simplification as

$$n_{ei,fd} = (\beta_0/e)T^3(m/2kT)^{1/2}\int_0^\infty \varepsilon_x^{-1/2}\left(\int_0^\infty \varepsilon f_{FD}(\varepsilon + \varepsilon_x)d\varepsilon\right)d\varepsilon_x. \tag{1c}$$

The momentum distribution of electrons, impinging the surface ($x = 0$) from inside having a total energy between ε and $(\varepsilon + d\varepsilon)$ and normal energy ε_x and $(\varepsilon_x + d\varepsilon_x)$, per unit area per unit time can be written as

$$n_{1,fd}(\varepsilon, \varepsilon_x)d\varepsilon d\varepsilon_x = (2kT\varepsilon_x/m)^{1/2} n_{e,fd}(\varepsilon, \varepsilon_x)d\varepsilon d\varepsilon_x$$

$$= (\beta_0/e)T^3(\varepsilon - \varepsilon_x)f_{FD}(\varepsilon)d\varepsilon d\varepsilon_x. \quad (2a)$$

The number of electrons having normal energy ε_x by imposing the limits in integral (Eq. (2a)) over the total energy as $\varepsilon \in (\varepsilon_x, \infty)$ and thus, using Eq. (2a), normal distribution of the electrons may be expressed as

$$n_{1,fd}(\varepsilon_x)d\varepsilon_x = (\beta_0/e)T^3\left(\int_{\varepsilon_x}^{\infty}(\varepsilon - \varepsilon_x)f_{FD}(\varepsilon)d\varepsilon\right)d\varepsilon_x$$

$$= (\beta_0/e)T^3\left(\int_{0}^{\infty}\varepsilon f_{FD}(\varepsilon + \varepsilon_x)d\varepsilon\right)d\varepsilon_x. \quad (2b)$$

After crossing the surface barrier height (W_a), the normal distribution of the electrons coming out can further be written by replacing the normal energy, $\varepsilon_x \rightarrow \varepsilon_x + w_a$, as

$$n_{1,fd}(\varepsilon_x)d\varepsilon_x = (\beta_0/e)T^3\left(\int_{0}^{\infty}\varepsilon f_{FD}(\varepsilon + \varepsilon_x + w_a)d\varepsilon\right)d\varepsilon_x. \quad (2c)$$

Furthermore, the barrier height of the quantum well (W_a) for graphene structures may be considered equivalent to the inherent work function ϕ (corresponding to Dirac point) of the single layered graphene, i.e., $W_a \approx \phi \equiv w_a \approx \varphi$ ($= e\phi/kT$); this may be different from the bulk graphite material. Using *f-d statistics* for the electrons available for emission, one gets

$$n_{1,fd}(\varepsilon_x)d\varepsilon_x = (\beta_0/e)T^3[-Polylog[2,$$
$$- \exp[-(\varepsilon_x + \varphi - \varepsilon_f)]]]d\varepsilon_x. \quad (3)$$

The notation $Polylog [u, v]$ in the above expression refers to the polylogarithm[56] function and can be expressed as power series $Li_u(v) = \sum_{l=1}^{\infty}(v^k/k^u)$. It should be mentioned here that Eq. (3) eventually infers the normal distribution of thermionic electrons, and thus, the distribution function (as $f_x d\varepsilon_x = n_{1,fd}(\varepsilon_x)d\varepsilon_x/n_{th}$) can be written by dividing this number by total net current. Integrating Eq. (3) over $\varepsilon_x \in (0, \infty)$, one obtains the outward flux of electrons from the plane surface ($x = 0$) and can be expressed as[57]

$$n_{ox,fd} = \int n_{1,fd}(\varepsilon_x)d\varepsilon_x = (\beta_0/e)T^3\int_{0}^{\infty}[-Polylog[2,$$
$$- \exp[-(\varepsilon_x + \varphi - \varepsilon_f)]]]d\varepsilon_x. \quad (4a)$$

If the surface is at the finite positive potential (V_s), which is anticipated in the steady state scenario, the emitted electrons leaving the surface with the normal energy less than $-v_s$ ($\approx eV_s/kT$) will get recollected over the surface. The flux associated with incoming electrons can thus be expressed as

$$n_{ix,fd} = \int_{0}^{-v_s} n_{1,fd}(\varepsilon_x)d\varepsilon_x = \left(\int_{0}^{\infty}n_{1,fd}(\varepsilon_x)d\varepsilon_x - \int_{-v_s}^{\infty}n_{1,fd}(\varepsilon_x)d\varepsilon_x\right). \quad (4b)$$

Hence, the net flux coming outward from the positively charged surface can be written as

$$n_{th,fd} = (n_{ox,fd} - n_{ix,fd}) = \int_{-v_s}^{\infty} n_{1,fd}(\varepsilon_x)d\varepsilon_x$$

$$= (\beta_0/e)T^3\int_{-v_s}^{\infty}[-Polylog[2, -\exp[-(\varepsilon_x + \varphi - \varepsilon_f)]]]d\varepsilon_x. \quad (5)$$

The above expression (Eq. (5)) refers to the electron flux coming out just on the surface of the graphene sheet and illustrates the T^3 dependence in contrast to the usual RD law; a similar conclusion has been drawn by Ang and Ang[47] in the case of multilayer graphene. In order to determine its spatial dependence, now consider a virtual plane parallel to the actual surface, characterized by the electric potential V and the normal energy ε'_x; and using the simple transformation between the two layers $\varepsilon'_x + v = \varepsilon_x + v_s \Rightarrow \varepsilon_x = (\varepsilon'_x + v - v_s)$, with $v = (-eV/kT)$. Substituting for ε_x in terms of virtual normal energy ε'_x in Eqs. (2)–(5) and proceeding as in the case of the surface ($x = 0$), the electron energy distribution and flux corresponding to the surface at an electric potential V is given by

$$n_{1,fd}(\varepsilon'_x)d\varepsilon'_x = (\beta_0/e)T^3[-Polylog[2,$$
$$- \exp[-(\varepsilon'_x + \varphi - \varepsilon_f + v - v_s)]]]d\varepsilon_x, \quad (6)$$

$$n_{ox,fd} = \int n_{1,fd}(\varepsilon'_x)d\varepsilon'_x = (\beta_0/e)T^3\int_{0}^{\infty}[-Polylog[2,$$
$$- \exp[-(\varepsilon'_x + \varphi - \varepsilon_f + v - v_s)]]]d\varepsilon_x, \quad (7a)$$

$$n_{ix,fd} = \int_{0}^{-v} n_{1,fd}(\varepsilon'_x)d\varepsilon'_x$$

$$= \left(\int_{0}^{\infty}n_{1,fd}(\varepsilon'_x)d\varepsilon'_x - \int_{-v}^{\infty}n_{1,fd}(\varepsilon'_x)d\varepsilon'_x\right), \quad (7b)$$

$$n_{th,fd} = (n_{ox,fd} - n_{ix,fd}) = (\beta_0/e)T^3\int_{-v}^{\infty}[-Polylog[2,$$
$$- \exp[-(\varepsilon'_x + \varphi - \varepsilon_f + v - v_s)]]]d\varepsilon'_x$$
$$= (\beta_0/e)T^3\int_{-v_s}^{\infty}[-Polylog[2, -\exp[-(\varepsilon_x + \varphi - \varepsilon_f)]]]d\varepsilon_x. \quad (8)$$

Comparing the expressions from Eqs. (8) and (5), it is evident that the net outward flux of electrons is the same at all virtual planes (all $v's$), which is just indicative of a steady state. The electron densities corresponding to the outward and inward electron fluxes can be written as[57]

$$n_{eo,fd} = \int dn_{eo,fd} \approx \int_{0}^{\infty}[n_{1,fd}(\varepsilon'_x)dn_x/v_x]d\varepsilon'_x$$

$$= (\beta_0/e)T^3(m_e/2kT)^{1/2}\int_{0}^{\infty}f_x d\varepsilon'_x, \quad (9a)$$

$$n_{ei,fd} = \int dn_{ei,fd} \approx \int_{0}^{-v}[n_{1,fd}(\varepsilon'_x)dn_x/v_x]d\varepsilon'_x$$

$$= (\beta_0/e)T^3(m_e/2kT)^{1/2}\int_{0}^{-v}f_x d\varepsilon'_x, \quad (9b)$$

where $f_x = \varepsilon'^{-1/2}_x[-Polylog[2, -\exp[-(\varepsilon'_x + \varphi - \varepsilon_f + v - v_s)]]]$.

Therfore, the net electron density at any virtual layer in the sheath can be written as

$$n_e = (n_{eo,fd} + n_{ei,fd}) = (\beta_0/e)T^3(m/2kT)^{1/2}\Upsilon_{fd}(v,v_s) \quad (10a)$$

or

$$(n_e/n_{e0}) = \Upsilon_{fd}(v,v_s)/\Upsilon_{fd}(v_s = 0). \quad (10b)$$

Here, $\Upsilon_{fd}(v,v_s) = [\int_0^\infty f_x d\varepsilon_x' + \int_0^{-v} f_x d\varepsilon_x']$ and $n_{e0} = (\beta_0/e)T^3(m/2kT)^{1/2}\Upsilon_{fd}(v_s = 0)$ represent the electron density on the uncharged plane surface.

Spatial dependence of sheath potential:

The space profile of the surface potential is determined by the Poisson equation, and corresponding to the thermionic sheath, it can be expressed as[57,58]

$$(d^2V/dx^2) = 4\pi n_e e \Rightarrow (d^2v/d\varsigma^2) = -(n_e/n_{e0})$$
$$= -\Upsilon_{fd}(v,v_s)/\Upsilon_{fd}(v_s = 0), \quad (11)$$

where $\varsigma = (x/\lambda_d)$ and $\lambda_d = (4\pi n_{e0,fd}e^2/kT)^{-1/2}$.

Equation (11) can be solved by using familiar steps, as multiplying both sides by $(2dv/d\varsigma)$ and using suitable boundary conditions, viz., $v'(\varsigma) = 0$ and $v(\varsigma) = 0$ as $\varsigma \to \infty$, obtaining

$$(dv/d\varsigma)^2 = -2\int[\Upsilon_{fd}(v,v_s)/\Upsilon_{fd}(v_s = 0)]dv = [\Lambda_{fd}(v)]^2. \quad (12a)$$

Only the positive square root of $(dv/d\varsigma)^2$ is physically tenable. Integrating the above expression (Eq. (12a)) with the boundary condition $v(\varsigma) = v_s$ as $\varsigma \to 0$, one gets

$$d\varsigma = \left(\frac{dv}{\Lambda_{fd}(v,v_s)}\right) \Rightarrow \varsigma = \int_{v_s}^v [1/\Lambda_{fd}(v,v_s)]dv. \quad (12b)$$

The expressions (Eqs. (11) and (12)) refer to the thermionic sheath features in terms of potential and density profile. Next, we discuss a simplified case when *f-d* statistics approaches the Maxwellian distribution of electrons.

B. A simplification

While considering the graphene surface operation at high temperature, it is reasonable to assume that only high energy contributions in the distribution are important for the electron emission, and thus, *f-d* statistics can be approximated as the typical Maxwellian distribution.[49] Empirically, in this case $(\varepsilon - \varepsilon_F) > 1$ should be much larger than unity, and hence, one can approximate *f-d* distribution of electrons as Maxwellian distribution, viz., $f_{FD}(\varepsilon) \sim f_M(\varepsilon) = \exp[-(\varepsilon - \varepsilon_F)]$. Following approach similar to the previous case with this simplification, Eqs. (6)–(8) can be simplified as[57]

$$n_{1,M}(\varepsilon_x')d\varepsilon_x' = (\beta_0/e)T^3 \exp[-(\varepsilon_x' + \varphi - \varepsilon_f + v - v_s)]d\varepsilon_x, \quad (13)$$

$$n_{ox,M} = \int_0^\infty n_{1,M}(\varepsilon_x')d\varepsilon_x' = (\beta_0/e)T^3 \exp[-(\varphi - \varepsilon_f + v - v_s)], \quad (14a)$$

$$n_{ix,M} = \int_0^{-v_s} n_{1,M}(\varepsilon_x')d\varepsilon_x'$$
$$= (\beta_0/e)T^3 \exp[-(\varphi - \varepsilon_f + v - v_s)][1 - \exp(v)], \quad (14b)$$

$$n_{th,M} = (n_{ox,M} - n_{ix,M}) = \int_{-v}^\infty n_{1,M}(\varepsilon_x')d\varepsilon_x'$$
$$= (\beta_0/e)T^3 \exp[-(\varphi - \varepsilon_f - v_s)]. \quad (15)$$

One can easily notice from this expression that the electron emission rate in the case of the monoatomic planar sheet is significantly different from the expression for bulk material, where it follows Richardson-Dushman (*RD*) law[59] as $n_{th,M} = (A_0/e)T^2 \exp[-(\varphi - v_s)]$, with the coefficient $A_0 = (4\pi emk^2/h^3) \sim 118A/cm^2 K^2$.

The electron densities corresponding to the outward and inward fluxes can be written as

$$n_{eo,M} = \int_0^\infty (dn_x/v_x)d\varepsilon_x'$$
$$= (\beta_0/e)T^3(m/2kT)^{1/2}\pi^{1/2}\exp[-(\varphi - \varepsilon_f + v - v_s)], \quad (16a)$$

$$n_{ei,M} = \int_0^{-v} (dn_x/v_x)d\varepsilon_x'$$
$$= (\beta_0/e)T^3(m/2kT)^{1/2}\pi^{1/2}$$
$$\times \exp[-(\varphi - \varepsilon_f + v - v_s)]erf[(-v)^{1/2}]. \quad (16b)$$

Net electron density at any layer in sheath can thus be written as

$$n_e = (n_{eo,M} + n_{ei,M}) = (\beta_0/e)T^3(m/2kT)^{1/2}$$
$$\times \exp[-(\varphi - \varepsilon_f + v - v_s)]\pi^{1/2}[1 + erf[(-v)^{1/2}]] \quad (17a)$$

or

$$(n_e/n_{e0}) = \exp(v_s - v)\Upsilon_M(v,v_s), \quad (17b)$$

where $n_{e0} = (\beta_0/e)T^3(m/2kT)^{1/2}\pi^{1/2}\exp[-(\varphi - \varepsilon_f)]$.

Using the simplified expression for the electron density (Eq. (18)) with the Poisson equation (similar to Eq. (11)), the potential gradient (i.e., field) and corresponding potential variation can be expressed as

$$\Lambda_M(v) = [2\exp(v_s)[[1 + erf[(-v)^{1/2}]]$$
$$\times \exp(-v) - 2\pi^{-1/2}(-v)^{1/2}]]^{1/2} \quad (18a)$$

and

$$\varsigma = \int_{v_s}^v [1/\Lambda_M(v,v_s)]dv. \quad (18b)$$

In the above analysis (Sections II A and II B), the electron flux (n_{th}), potential (v), and electron density (n_e/n_{e0}) in the sheath have been derived as a function of ($v_s - v$), and hence the normalized spatial distance (ς); these parameters effectively describe the electron sheath over the graphene surface. The results of the two cases, viz., *f-d* and *Maxwellian* statistics along with other relevant parameters have been obtained

by solving appropriate equations/expressions and the results are graphically illustrated in the later part.

III. THERMIONIC CONVERTER (TC) CONFIGURATION

Here, we consider a TC configuration accomplishing direct conversion using thermionic electron flux liberated from the single layered graphene based cathode. In the conversion scheme, the emission current is condensed over a metal based collector having lower work function $\phi_C(<\phi_E)$ and maintained at a lower temperature $T_C(\ll T_E)$, so that the back emission from the collector can be minimized; usually, the emitter plate is kept at the negative potential with respect to the anode.[4] The electronic circuit is completed via an external load across which electrical power may be extracted. Physically, in addition to the anode potential, the thermodynamic force due to the temperature gradient in the gap collects electrons and guides them from emitter to collector. According to the energy balance of TCs, the net input thermal flux can be expressed as[4,60]

$$P_{in} = [J_E(\phi_E + 2kT_E) - J_C(\phi_C + 2kT_C)]. \qquad (19)$$

In this expression (Eq. (19)), $J_E\phi_E(J_C\phi_C)$ refers to the energy flux consumed in liberating the electrons from the Fermi level of the emitter (collector) plate, while $\sim 2kT_E$ ($2kT_C$) corresponds to the mean thermal energy of the electrons after emission from the cathode (anode) surface, J_E ($= en_{th,E}$) and $J_C(= en_{th,C})$ are surface current densities associated with the electron flux (n_{th}) from the emitter ($n_{th,E}$) and collector ($n_{th,E}$) plates; in writing Eq. (19), other energy loss processes (like radiation cooling/collisions) are ignored. The net current across the emitter-collector in TC setup is $J_{EC}(=J_E - J_C)$, and following Rasor,[4] the optimal thermal energy appearing as output power across the load ($\phi_{EC} = \phi_E - \phi_C$) can be written as

$$P_{out} = J_{EC}\phi_{EC} = (J_E - J_C)(\phi_E - \phi_C). \qquad (20)$$

By ignoring the space charge effects, the expression for efficiency of TCs can be written as[4]

$$\chi = P_{out}/P_{in} = [J_{EC}\phi_{EC}/[J_E(\phi_E + 2kT_E) - J_C(\phi_C + 2kT_C)]]. \qquad (21)$$

It is interesting to note here that the numerator of the expression for conversion efficiency (Eq. (21)) includes two competing terms, namely, J_{EC} and ϕ_{EC} which may signify the optimization of the conversion efficacy. In conventional TCs, the current reaching the collector plate is limited due to space charge and effectively degrades the output power across the load. The expressions for the current derived herein do not include this screening effect, as it only depends on lattice properties and ideally applicable to the case space charge free regime. As the space charge field becomes effective, it suppresses the emission current from the emitter, which results in TC being operated in the space charge limited regime. Applying a positive potential over the collector plate eventually eases the flow of electrons by overcoming the space charge field and apparently makes the TC to

operate in the space charge free regime. This effect is taken care of by Child's law which estimates the space charge limited current to the collector plate as $J_a \sim \kappa V_{EC}^{3/2}/d^2$, where V_{EC} and d refer to the potential and mean distance across the electrodes while κ is a constant; the relation implies that the space charge effect can be suppressed by operating the anode at positive potential and minimizing the emitter-collector separation.[60,61] In our present work, we have not considered the case when the external potential is applied to the collector plate. The insertion of the current controlling grid[60] and filling of Cs Oxygen vapor plasma in between the emitter and collector plates are a few of the other efficient processes to optimize the effect of the space charge.[4] In the present analysis, this effect of the space charge may be physically included in the analysis by inserting a finite potential drop due to the space charge loss (ΔV) in the emitter (cathode) barrier index, viz., ($\phi_E + \Delta V$) in determining the thermionic flux from the emitter plate (J_E); in the moderate range of the electron flux (~ 1 A/cm^2) from the emitter, ΔV acquires the small value[4] $\sim$(0.1–0.5) V. Taking account of the appropriate set of parameters for configuring TCs, the results for efficiency have been graphically illustrated and discussed.

IV. NUMERICAL RESULTS AND DISCUSSION

A. Emission current and sheath formation from single layer graphene sheet

In this subsection, we analyze the numerical results based on the analytical expressions for the electron emission and respective sheath structure due to the thermionic emission of electrons from the monoatomic graphene layer operating at high temperature. It is interesting to note that the thermionic emission current based on the f-d statistics predicts marginally smaller magnitude in comparison to the simplified solution obtained considering the Maxwellian distribution of the electrons (i.e., Eq. (16)); the ratio ($R_{fd,M}[=n_{th,fd}/n_{th,M}]$) of the thermionic emission currents in the two cases (using Eqs. (5) and (16)) has been displayed as a function of $\delta(=\varphi - \varepsilon_f)$ for different values of surface potential υ_s in Fig. 1. The figure indicates that the expression based on the Maxwellian distribution of electrons overestimates the thermionic emission current for smaller $\delta(<5)$ values, while this is reasonably a good approximation for larger $\delta(\geq 5)$, as the flux ratio approaches unity; the difference primarily originates from the nature of the two distribution functions. It is also discerned that the expression for thermionic emission flux from the thin monoatomic layer is significantly different from the usual RD law applicable for the bulk material. The difference between the emission currents in the two cases, viz., RD law and present 2-d analysis, has been displayed as a function of a material work function for different values of surface temperature in Fig. 2(a). It is noticed that the RD law predicts a larger thermionic flux at smaller temperature ($\sim$1200 K), while a reverse trend is observed with the increasing temperature ($\sim$2000 K); both the estimates predict approximately the same flux for temperature $\sim$1500 K. This nature can be attributed to the ignorance of the Fermi energy configuration and its temperature dependence in the usual RD formulation; these intrinsic
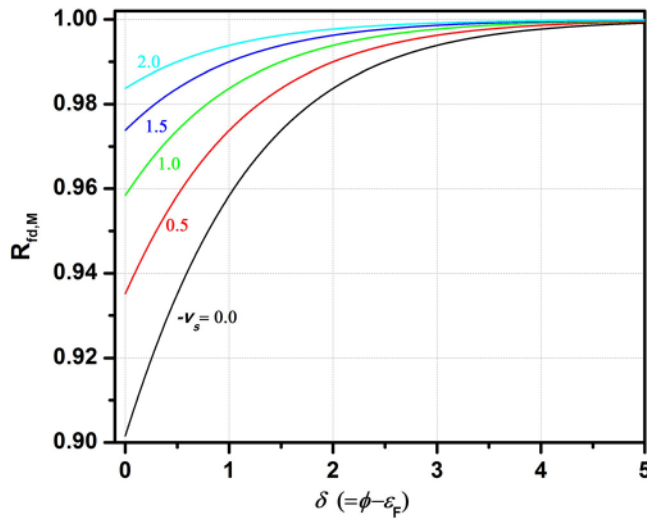
FIG. 1. The ratio $R_{fd,M}$ as a function of $\delta(=\varphi - \varepsilon_f)$ for different values of the dimensionless surface potential v_s; the labels of varying parameters are indicated on the curves.

features are considered in the present analysis. Conclusively, the estimates based on the present analysis deviates from the usual RD behaviour in low and high temperature regimes. Furthermore, due to the increasing barrier height for emission, the thermionic flux is seen to decrease with the increasing material work function in both the cases. The expressions for the thermionic flux and consequent sheath parameters derived herein significantly depend on the material work function, Fermi level, surface temperature, and surface potential. Before utilizing the present analysis for the calculations, it is customary to verify the applicability of the analytical expressions towards the monoatomic layered structures; for this, we take note of a recent experimental work by Zhu et al.[50] In this work, using the method of thermionic emission, the work function of the single layer polycrystalline graphene sheet (specifically $\sim 15\,mm^2$), operating in high temperature regime ($\sim 1200\,K$) is specified to vary in the range of $\phi = (4.74 \pm 0.04)\,eV$. The analytical results for the thermionic emission current from the uncharged (viz., $v_s = 0$) monoatomic layer graphene sheet corresponding to the three values of work functions (i.e., 4.7 eV, 4.74 eV, and 4.8 eV) and tuned intrinsic Fermi energy level ($E_F \sim 0.055\,eV$ at room temperature $\sim 300\,K$) with its linear temperature dependence[38] have been illustrated in Fig. 2(b); the experimental data for the thermionic emission current[48,50] from the graphene sheet has been marked by the blue dots. The analytical estimate based on f-d statistics (Eq. (5)) is in a good agreement with the experimental results for the thermionic flux (see Fig. 2(b)). The broken curves correspond to the usual RD law prediction for the emission current from the bulk material and are seen to underestimate in comparison to the present 2-d analysis. However, the RD prediction is also noticed to fit reasonably with the experimental data for $\phi = 4.7\,eV$ but it should be noted that the RD formulation does not include the inherent features (like Fermi level and its temperature dependence) of graphene, and hence, its utility in the present context (2-d monolayer graphene sheet) is physically imprecise. As mentioned earlier that advanced surface engineering[30–32]
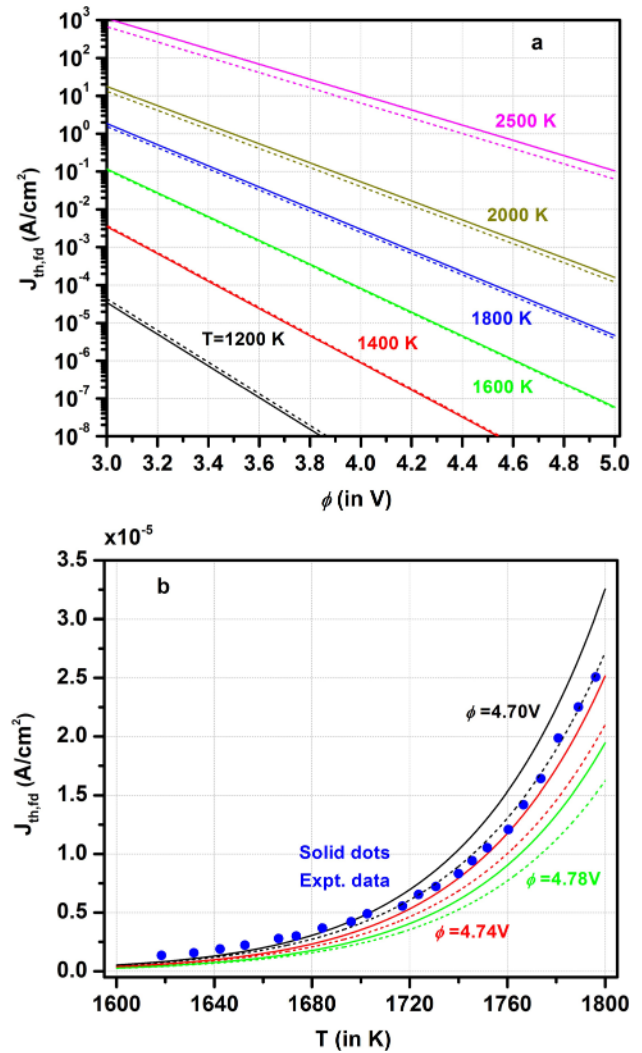

FIG. 2. (a) Thermionic flux ($J_{th,fd}$) as a function of the material work function for different values of surface temperature (T) and $E_F = 0.055\,eV$ (at 300 K); the solid and broken curves refer to the present analysis and the usual RD estimate, respectively. (b) Comparison with experimental data:[50] thermionic flux ($J_{th,fd}$) as a function of the surface temperature corresponding to the graphene sheet for $\phi = (4.74 \pm 0.04)\,eV$ and $E_F = 0.055\,eV$ at 300 K, while the blue dots refer to the experimental measurements; the solid and broken curves refer to the present analysis and usual RD estimate, respectively. The labels are indicated on the curves.

elucidates the possibility of fabricating the graphene sheet with the desired features, the work function in the literature is reported to vary in the range ~ 3.7–$5.2\,eV$, while the intrinsic Fermi level may be tuned in the range ~ 0.01–$1.0\,eV$ by various technological means.[48] Hence, after validating the analytical expression, it is worth illustrating the parametric variation of the thermionic emission current from the graphene sheet; these effects for the wide range of work function and Fermi level corresponding to the uncharged ($v_s = 0$) surface are shown in Figs. 3(a) and 3(b), respectively. The decrease in the thermal flux with increasing work function and decreasing Fermi level is primarily a consequence of the effective increase in the barrier height to overcome by electrons in the emission process. In case, the surface is at finite positive potential, it puts forward an additional barrier for the electrons coming out from the surface and results in decreasing thermionic flux; this behavior is shown in Fig. 4.

Next, we discuss the formation of the sheath by thermionic electron cloud in the steady state, in the proximity of top of the positively charged surface. Concerning the graphene sheet operating at large temperature (as $\delta > 5$) in the present context, the simplified expressions (i.e., Eq. (18)) are used in illustrating the steady state sheath properties. The sheath potential (v/v_s) and corresponding electron density (n_e/n_{e0}) as a function of dimensionless spatial distance ($\varsigma = x/\lambda_d$) for different $v_s (= eV_s/kT)$ values have been illustrated in Fig. 5. As displayed in Fig. 5(a), the sheath potential acquires larger magnitude for large values of v_s at a given ς and it is seen to sustain for longer spatial distance (ς). The corresponding space profile of the dimensionless electron density (n_e/n_{e0}) in the thermionic sheath is noticed to extend up to $\sim 10\lambda_d$ and weakly depends on the surface potential v_s (see Fig. 5(b)). It should be mentioned here that the expressions based on f-d statistics (Eq. (12)) are equally applicable in this case and have been verified to give the same results. For the graphene sheet in the present context ($\varphi \sim 4.74\,\text{eV}$ and $E_F \sim 0.055\,\text{eV}$) operating at high temperature ($T \sim 1500\,\text{K–}2000\,\text{K}$), the normalization units, i.e., $n_{e0} \in$
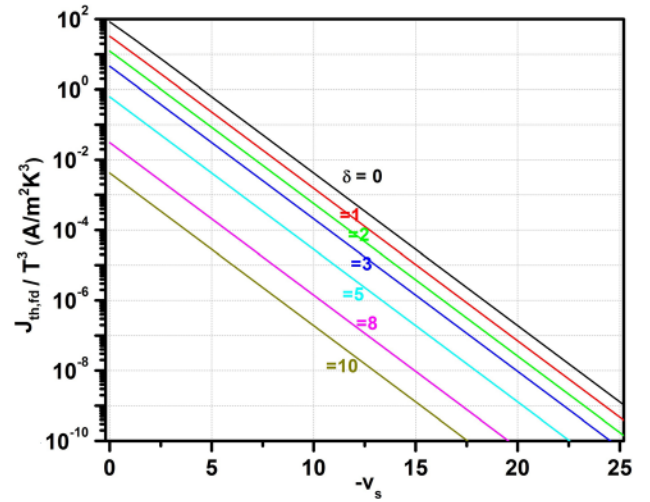
FIG. 4. Thermionic flux ($J_{th,fd}/T^3$) as a function of the dimensionless surface potential ($-v_s$) for different values $\delta (= \varphi - \varepsilon_f)$; the labels of varying parameters are indicated on the curves.

$(8.2 \times 10^3 - 1.6 \times 10^8)\,\text{cm}^{-3}$ and $\lambda_d \in (2.95 - 0.025)\,\text{cm}$ are noticed to vary in a wide range; these normalizing parameters are displayed in Fig. 5(c) for different values of the intrinsic Fermi level (E_F). This suggests that the sheath potential and respective sheath density in real units fall faster for the graphene sheet operating at a large temperature.

B. TCs configuration using graphene sheet

In order to examine the feasibility of 2d-graphene monoatomic layer towards TCs, we consider using it as a graphene based cathode with the metallic anode in configuring the TC setup. In this setup, the cathode is usually kept at negative bias and higher temperature with respect to the anode (collector) plate. In this context, we use the expression (Eq. (5)) derived herein (for the uncharged surface, i.e., $v_s = 0$) in evaluating the thermionic current (J_E) from the graphene sheet cathode. The usual RD law has first been amended by applying f-d statistics and then applied to evaluate the return current from the bulk metallic anode operating at a relatively lower temperature. As evident from the expression of TC's conversion efficiency (Eq. (21)), it primarily depends on the work function and thermionic currents from the cathode/anode plates. Thus, here we analyze the dependence of TC's efficiency on different operating parameters by varying temperature and work functions of the emitter/collector plates, intrinsic Fermi level of graphene, and including space charge effects by varying emitter barrier index. For computations, the following standard parameters for TC setup are used: $T_E = 1200\,\text{K}$, $E_F = 0.055\,\text{eV}$, and $\phi_E = 4.74\,\text{eV}$ (corresponding to graphene based cathode), $T_C = 400\,\text{K}$, $\phi_C = 2.0\,\text{eV}$ (for the metallic anode), and $\Delta V = 0$ (space charge barrier index); the effect of the individual parameter on efficiency is evaluated by varying it over a range and keeping the other the same.

The dependence of conversion efficiency on the emitter temperature (T_E) for different values of anode potential (solid lines) and intrinsic Fermi level (broken lines) has been displayed in Fig. 6(a). For a given E_F, the efficiency is seen
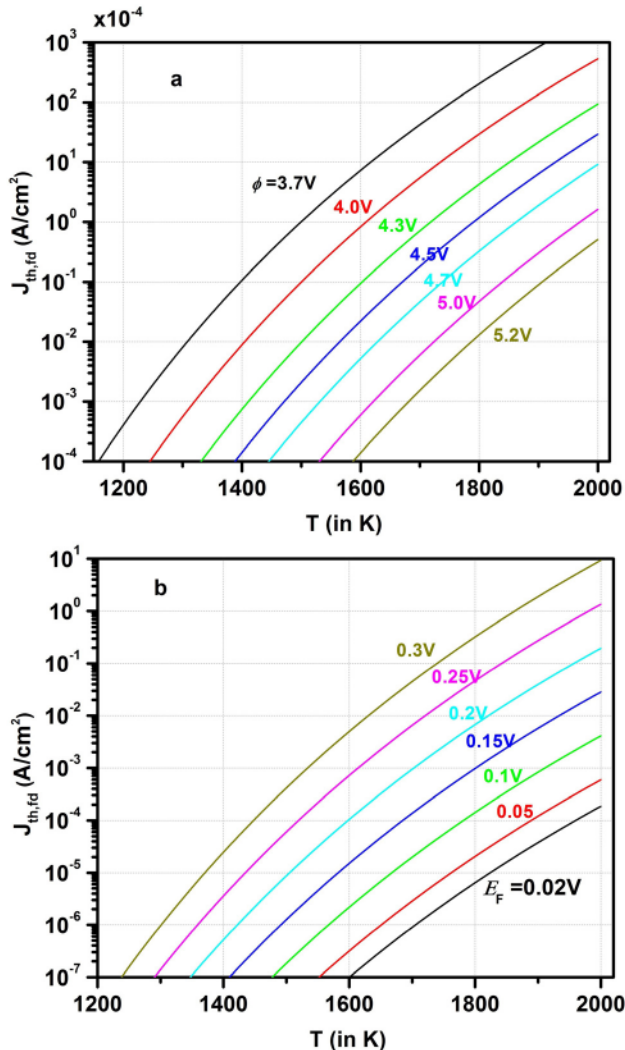

FIG. 3. Thermionic current from the thin graphene sheet ($J_{th,fd}$) as a function of the surface temperature for different values of (a) work functions (ϕ) and (b) intrinsic Fermi level (E_F); the labels are indicated on the curves.

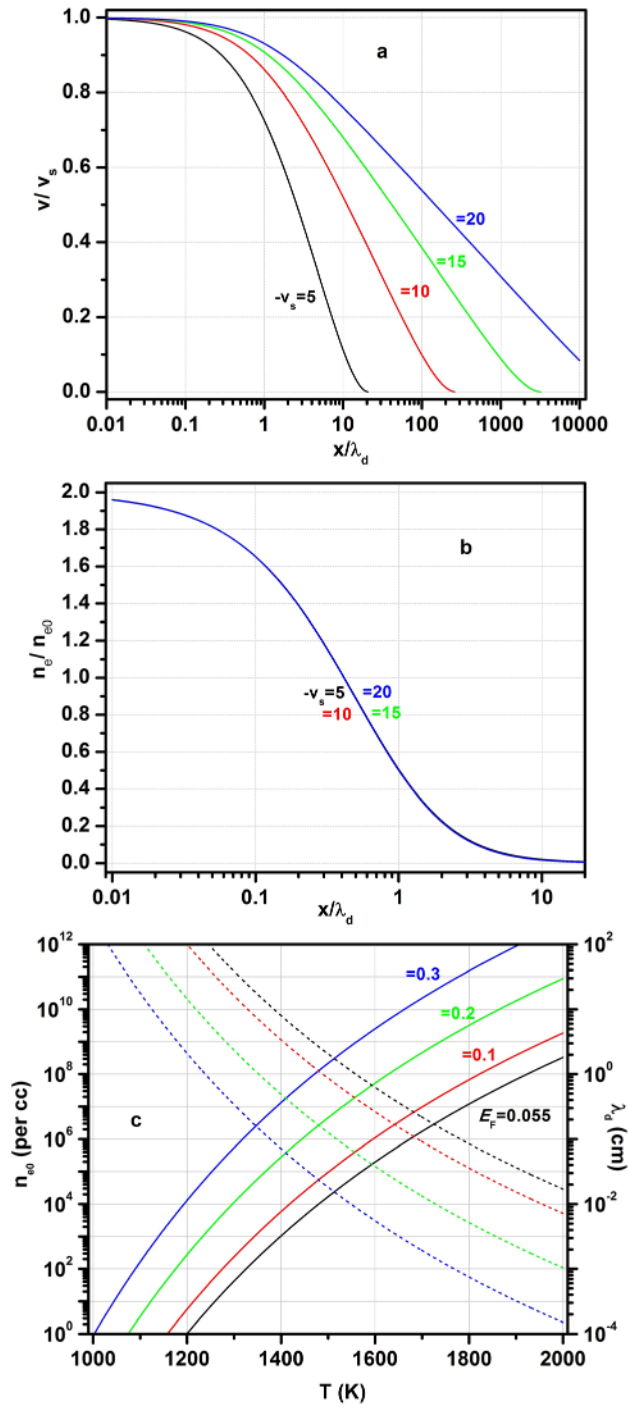FIG. 5. Thermionic sheath structure over the thin graphene sheet: (a) dimensionless potential $v/v_s (\approx V/V_s)$ and (b) respective dimensionless electron density (n_e/n_{e0}) as a function of $\varsigma (= x/\lambda_d)$ for different values of the surface potential ($-v_s$). (c) The normalizing parameters n_{e0} (left hand scale, solid lines) and λ_d (right hand scale, broken scale) as a function of surface temperature for different values of intrinsic Fermi level (E_F). The labels of varying parameters are indicated on the curves.

optimum efficiency (χ_{opt}), but the TC achieves optimum conversion efficiency at the lower cathode temperature in the case of higher E_F. As evident from Fig. 6(b), the conversion efficiency depends critically on the anode temperature and sharply reaches a minimum value at a threshold anode temperature ($T_{C,thr}$). This nature can be understood in terms of decrease in the net current flowing across the load in the external circuit (i.e., J_{EC}). This threshold temperature ($T_{C,thr}$) increases with the increasing operating temperature of cathode plate (T_E); for the standard case, $T_{C,thr} \sim 525$ K is obtained. The effect of space charge on conversion efficiency has been explored in Fig. 7, where χ variation for different values of ΔV is depicted as a function of emitter/collector work function. As depicted in Fig. 7(a), the conversion efficiency takes an optimum value (χ_{opt}) in the low work function ($\phi_C \leq \phi_{C,opt}$) regime, and the TC setup is seen to specify the maximum efficacy $\chi_{opt} \sim 62\%$ ($\sim 0.93 \; \chi_{carnot}$) at around $\phi_C \sim 1.6$ eV. As anticipated earlier, this optimization
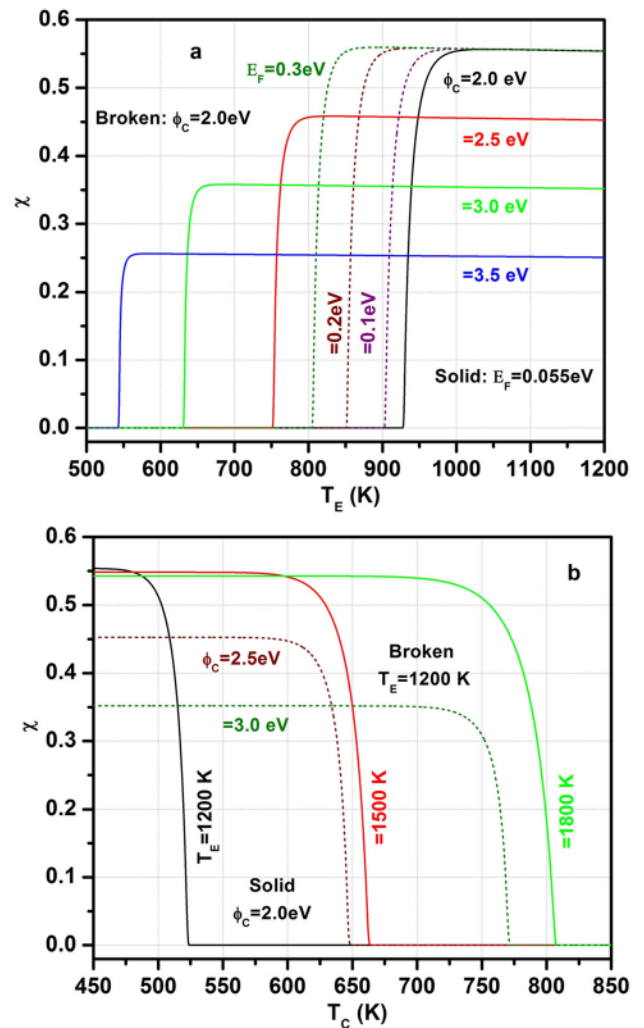

FIG. 6. (a) The conversion efficiency (χ) as a function of the temperature of emitter surface (T_E) for different values of anode work functions (ϕ_C, solid lines) and intrinsic Fermi level (E_F, broken lines); (b) χ as a function of collector surface (T_C) temperature for different values of anode work functions (ϕ_C, broken lines) and emitter temperature (T_E, solid lines); the curves refer to the graphene based cathode (emitter) work function $\phi_E = 4.74$ eV, intrinsic Fermi level $E_F = 0.055$ eV at 300 K and space charge index $\Delta V = 0$. The labels of varying parameters are indicated on the curves.
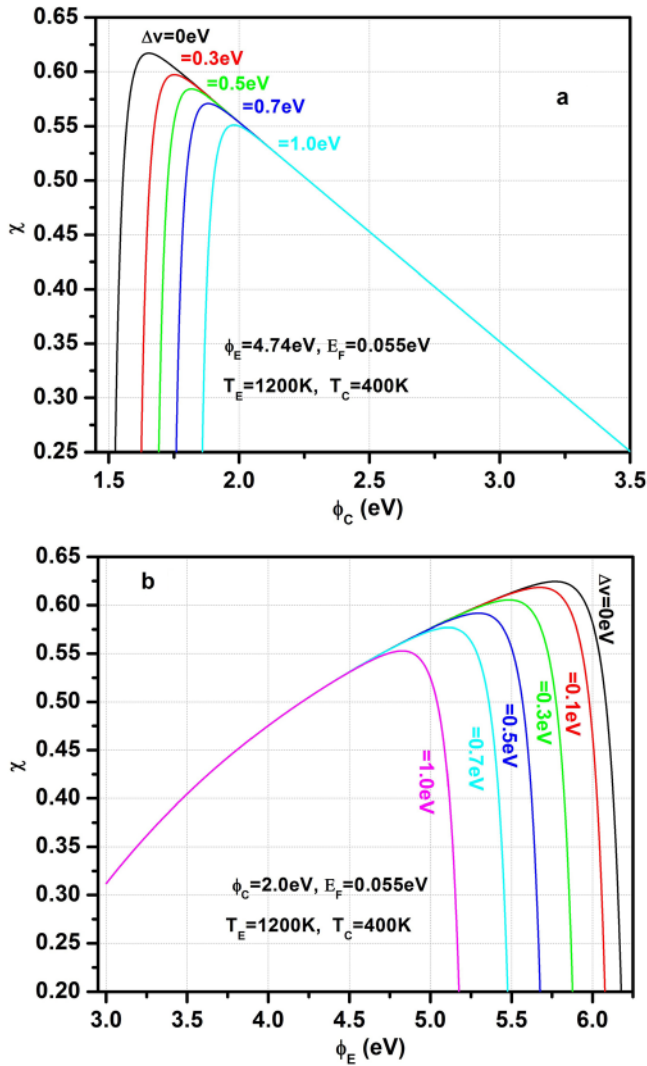
to decrease with the increasing work function of the metallic anode due to the decreasing ϕ_{EC}; however, it acquires an optimum value (χ_{opt}) at lower T_E. In particular, for the standard case, TC displays the conversion efficiency of $\sim 56\%$ which is approximately $\sim 84\%$ of the Carnot efficiency, i.e., $\chi_{carnot} = (1 - T_C/T_E) = 2/3$. However, the variation of Fermi level (E_F) is noticed to marginally influence the

FIG. 7. Conversion efficiency (χ) as a function of the work function of the (a) collector surface (ϕ_C) (b) cathode surface (ϕ_E) for different values of space charge index ΔV; the curves refer to the graphene based cathode (emitter) work functions $\phi_E = 4.74\,\text{eV}$, $T_E = 1200\,\text{K}$, intrinsic Fermi level $E_F = 0.055\,\text{eV}$ at 300 K, and anode work functions $\phi_C = 2.0\,\text{eV}$ and $T_C = 400\,\text{K}$. The labels of varying parameters are indicated on the curves.

is a consequence of the mutual competing terms of the net current (J_{EC}) reaching the collector, flowing across the load, and magnitude of optimal external load (ϕ_{EC}), which ultimately determine the conversion efficiency. Consequently, the decrease in χ with increasing $\phi_C (> \phi_{C,opt})$ and its sharp decay below $\phi_{C,opt}$ can also be explained where the alternative terms, viz., ϕ_{EC} and J_{EC} become dominant over each other in the respective sections. The inclusion of space charge effect via ΔV (i.e., additional emitter barrier index) reduces the conversion efficiency, as its optimum value drops by $\sim 10\%$, as the barrier index $\Delta V \in (0, 1.0\,\text{eV})$; this behavior is a consequence of the decreasing electron flux reaching the collector (anode) plate in overcoming an extra potential barrier ΔV in addition to ϕ_E. Furthermore, $\phi_{C,opt}$ is also noticed to increase with increasing space charge effect. The effect of varying the work function (ϕ_E) of the cathode (emitter) surface on the conversion efficiency has been illustrated in Fig. 7(b), and similar to the previous case (Fig. 7(a)), it also displays the optimum efficacy corresponding to

$\phi_E \approx \phi_{E,opt}$. It is again a consequence of ϕ_E dependence of net current reaching at anode plate (J_{EC}) and optimal external load (ϕ_{EC}). The cathode work function ($\phi_{E,opt}$) corresponding to the optimum value of χ (i.e., χ_{opt}) is noticed to shift towards the smaller ϕ_E values with increasing ΔV. These analytical results indicate that even TCs with $\sim 62\%$ of the conversion factor ($\sim 90\%$ of the Carnot efficiency) can be achieved via appropriate parametric tuning of the graphene sheet (cathode) and metallic collector (anode). Hence, with such TC configuration, a good fraction of the input flux can be converted into electrical energy.

V. SUMMARY

In summary, utilizing appropriate densities of the state configuration, Fermi Dirac (f-d) statistics for the energy distribution of electrons and Poisson equations along with the *Fowlers* treatment of the electron emission, a formalism describing the thermionic emission from the monoatomic graphene layer, operating at finite temperature and the consequent formation of the thermionic sheath in the proximity of graphene surface, have been established. The pertinence of the analytical expression for the thermionic flux has been validated with the recent experimental results for the 2d-single graphene layer, and the analytical predictions are found to be in good agreement. The steady state potential structure and the electron density spatial profile in the thermionic sheath have been analytically derived and the numerical results corresponding to graphene parameters are graphically presented; the electron sheath is shown to have a span of few (~ 10s) Debye lengths. The feasibility of such monolayer structures in utilizing it as graphene based cathode in a TC configuration has been explored. The conversion efficiency has parametrically been examined as a function of the constituent TC (anode/cathode, space charge) parameters and the appropriate operating regime has been identified; the conversion efficiency is noticed to acquire optimum value for cathode/anode material work functions. Further parametric tuning, for example, tweaking of the graphene work function to the desired extent via various technological means, such as intercalation,[62,63] electron (or hole) doping,[64] and electric field methods,[65] may also improve the conversion efficiency, as illustrated in the figures. In an illustrative case, a TC operating with the graphene based cathode ($T_E = 1200\,\text{K}$) and metallic collector ($T_C = 400\,\text{K}$, $\varphi_C = 2.0\,\text{eV}$) has been shown to display the conversion efficiency of $\sim 56\%$ which infers approximately $\sim 84\%$ of Carnot efficiency. This ensures the utility of the graphene based cathode as a promising contrivance in improving the conversion efficiency for TCs, and hence, in accomplishing the significant fraction of the thermal flux conversion into electrical energy.

[1]G. N. Hatsopoulos and E. P. Gyftopoulos, *Thermionic Energy Conversion*: Vol. 1: Processes and Devices (MIT Press, Cambridge, 1974).
[2]S. W. Angrist, *Direct Energy Conversion* (Allyn and Bacon, USA, 1976).
[3]G. N. Hatsopoulos and E. P. Gyftopoulos, *Thermionic Energy Conversion*: Vol. 2: Theory, Technology and Applications (MIT Press, Cambridge, 1979).
[4]N. S. Rasor, IEEE Trans. Plasma Sci. **19**, 1191 (1991).

[5]M. G. Kanatzidis, S. D. Mahanti, and T. P. Hogan, *Chemistry, Physics and Materials Science of Thermoelectric Materials* (Kluwer, New York, 2003).

[6]T. M. Tritt, M. A. Subramanian, H. Bottner, T. Caillat, G. Chen, R. Funahashi, X. Ji, M. Kanatzidis, K. Koumoto, G. S. Nolas, J. Poon, A. M. Rao, I. Terasaki, R. Venkatasubramanian, and J. Yang, MRS Bull. **31**, 188 (2006).

[7]H. Xi, L. Luo, and G. Fraisse, "Development and applications of solar-based thermoelectric technologies," Renewable Sustainable Energy Rev. **11**, 923 (2007).

[8]G. J. Snyder and E. S. Toberer, Nat. Mater. **7**, 105 (2008).

[9]S. B. Riffat and X. Ma, "Thermoelectrics: A review of present and potential applications," Appl. Therm. Eng. **23**, 913 (2003).

[10]K. A. A. Khalid, T. J. Leong, and K. Mohamed, "Review on thermionic energy converters," IEEE Trans. Electron Devices **63**, 2231 (2016).

[11]G. Schierning, R. Chavez, R. Schmechel, B. Balke, G. Rogl, and P. Rogl, Trans. Mater. Res. **02**, 025001 (2015).

[12]J. Zhang, H. J. Liu, L. Cheng, J. Wei, J. H. Liang, D. D. Fan, J. Shi, X. F. Tang, and Q. J. Zhang, Sci. Rep. **04**, 6452 (2014).

[13]S. Bathula, M. Jayasimhadri, B. Gahtori, N. K. Singh, K. Tyagi, A. K. Srivastava, and A. Dhar, Nanoscale **7**, 12474 (2015).

[14]S. Ihnatsenka, X. Crispin, and I. V. Zozoulenko, Phys. Rev. B **92**, 035201 (2015).

[15]W. Choi, D. Jun, S. Kim, M. Shin, and M. Jang, Energy **82**, 180 (2015).

[16]D. N. Kossyvakis, C. G. Vossou, C. G. Provatidis, and E. V. Hristoforou, Renewable Energy **81**, 150 (2015).

[17]M. Fisac, F. X. Villasevil, and A. M. Lopez, Renewable Energy **81**, 658 (2015).

[18]L. M. Shen, H. X. Chen, F. Xiao, and S. W. Wang, Energy Convers. Manage. **100**, 23 (2015).

[19]M. Kahaly, K. Ozdogan, and U. Schwingenschlogl, J. Mater. Chem. A **01**, 8406 (2013).

[20]C. Fu, S. Bai, Y. Liu, Y. Tang, L. Chen, X. Zhao, and T. Zhu, Nat. Commun. **06**, 8144 (2015).

[21]X. Zhang and L.-D. Zhao, J. Mater. **01**, 92 (2015).

[22]Y. Yan, G. Zhang, C. Wang, C. Peng, P. Zhang, Y. Wang, and W. Ren, Sci. Rep. **06**, 29550 (2016).

[23]T. Mori, Mater. Matters **04**, 37 (2009).

[24]K. S. Novoselov, A. K. Geim, S. V. Morozov, D. Jiang, Y. Zhang, S. V. Dubonos, I. V. Grigorieva, and A. A. Firsov, Nature **306**, 666 (2004).

[25]K. S. Novoselov, A. K. Geim, S. V. Morozov, D. Jiang, M. I. Katsnelson, I. V. Grigorieva, S. V. Dubonos, and A. A. Firsov, Nature **438**, 197 (2005).

[26]A. A. Balandin, S. Ghosh, W. Bao, I. Calizo, D. Teweldebrhan, F. Miao, and C. N. Lau, Nano Lett. **8**, 902 (2008).

[27]H. Raza, *Graphene Nanoelectronics: Metrology, Synthesis, Properties and Applications* (Springer, London, 2012).

[28]C. N. R. Rao and A. K. Sood, *Graphene: Synthesis, Properties, and Phenomena* (Wiley-VCH: Verlag, 2012).

[29]Y. Wu, Z. Shen, and T. Yu, *Two Dimensional Carbon: Fundamental Properties, Synthesis, Characterization and Applications* (Pan Stanford, Florida, 2014).

[30]S. Shafraniuk, *Graphene: Fundamentals, Devices, and Applications* (Pan Stanford, Florida, 2015).

[31]W. Choi and J.-W. Lee, *Graphene: Synthesis and Applications* (CRC Press, Florida, USA, 2016).

[32]See http://www.graphenea.com/ for properties of graphene and its applications.

[33]S. Sun, L. K. Ang, D. Shiffler, and J. W. Luginsland, Appl. Phys. Lett. **99**, 013112 (2011).

[34]X. Wei, D. Golberg, Q. Chen, Y. Bando, and L. Peng, Nano Lett. **11**, 734 (2011).

[35]S.-J. Liang, S. Sun, and L. K. Ang, Carbon **61**, 294 (2013).

[36]S.-J. Liang and L. K. Ang, IEEE Trans. Electron Devices **61**, 1764 (2014).

[37]X. Wei, S. Wang, Q. Chen, and L. Peng, Sci. Rep. **4**, 5102 (2014).

[38]M. F. Cracium, S. Russo, M. Yamamoto, and S. Tarucha, Nano Today **06**, 42 (2011).

[39]Y. Yin, Z. Cheng, L. Wang, K. Jin, and W. Wang, Sci. Rep. **04**, 5758 (2014).

[40]A. C. Walt, A. de Heer, and D. Ugarte, Science **270**, 1179 (1995).

[41]J.-M. Bonard, M. Croci, C. Klinke, R. Kurt, O. Noury, and N. Weiss, Carbon **40**, 1715 (2002).

[42]B. K. Sarker and S. I. Khondaker, ACS Nano **6**, 4993 (2012).

[43]Y. Cheng and O. Zhou, C.R. Phys. **4**, 1021 (2003).

[44]S.-D. Liang, N. Y. Huang, S. Z. Deng, and N. S. Xu, J. Vac. Sci. Technol. B **24**, 983 (2006).

[45]S.-D. Liang and L. Chen, Phys. Rev. Lett. **101**, 027602 (2008).

[46]S.-D. Liang and L. Chen, J. Vac. Sci. Technol. B **28**, C2A50 (2010).

[47]Y. S. Ang and L. K. Ang, Phys. Rev. Appl. **06**, 034013 (2016).

[48]S.-J. Liang and L. K. Ang, Phys. Rev. Appl. **03**, 014002 (2015).

[49]R. H. Fowler, *Statistical Mechanics: The Theory of the Properties of Matter in Equilibrium* (Cambridge University Press, London, 1955).

[50]F. Zhu, X. Lin, P. Liu, K. Jiang, Y. Wei, Y. Wu, J. Wang, and S. Fan, Nano Res. **7**, 553 (2014).

[51]P. R. Wallace, Phys. Rev. **71**, 622 (1947).

[52]F. Seitz, *Modern Theory of Solids* (McGraw-Hill Book Co., New York, 1940).

[53]A. H. C. Neto, F. Guinea, N. M. R. Peres, K. S. Novoselov, and A. K. Geim, Rev. Mod. Phys. **81**, 109 (2009).

[54]N. W. Ashcroft and N. D. Mermin, *Solid State Physics* (Harcourt College Publishers, New York, 1976).

[55]Z. Jiang, E. A. Henriksen, L. C. Tung, Y.-J. Wang, M. E. Schwartz, M. Y. Han, P. Kim, and H. L. Stormer, Phys. Rev. Lett. **98**, 197403 (2007).

[56]I. Stegun and M. Abramowitz, *Handbook of Mathematical Functions* (Dover Publications, New York, 1965).

[57]M. S. Sodha and S. K. Mishra, Phys. Plasmas **21**, 093704 (2014).

[58]S. Misra, S. K. Mishra, and M. S. Sodha, Phys. Plasmas **22**, 043705 (2015).

[59]M. S. Sodha, *Kinetics of Complex Plasmas* (Springer, New Delhi, 2014).

[60]J.-H. Lee, I. Bargatin, N. Melosh, and R. Howe, Appl. Phys. Lett. **100**, 173904 (2012).

[61]S. Meir, C. Stephanos, T. H. Geballe, and J. Mannhart, J. Renewable Sustainable Energy **5**, 043127 (2013).

[62]J.-K. Chang, W.-H. Lin, J.-I. Taur, T.-H. Chen, G.-C. Liao, T.-W. Pi, M.-H. Chen, and C.-I. Wu, ACS Appl. Mater. Interfaces **7**, 17155 (2015).

[63]T. P. Koloni, M. U. Kahaly, Y. C. Cheng, and U. Schwingenschlogl, J. Mater. Chem. **22**, 23340 (2012).

[64]J.-Y. Syu, Y.-M. Chen, K.-X. Xu, S.-M. He, W. C. Hung, C.-L. Chang, and C.-Y. Su, RSC Adv. **06**, 32746 (2016).

[65]Y.-J. Yu, Y. Zhao, S. Ryu, L. E. Brus, K. S. Kim, and P. Kim, Nano Lett. **09**, 3430 (2009).